Journal of Materials Chemistry C

ROYAL SOCIETY OF CHEMISTRY

PAPER

View Article Online
View Journal | View Issue

Cite this: J. Mater. Chem. C, 2024, 12, 11769

Synthesis, crystal structure, and physical properties of the Eu(II)-based selenide semiconductor: $EuHfSe_3$†

Subhendu Jana,[a] Shaun O'Donnell,[b] Ian A. Leahy,[b] Aylin Koldemir,[c] Rainer Pöttgen,[c] Rebecca W. Smaha[b] and Paul A. Maggard*[a]

Received 28th April 2024,
Accepted 7th July 2024

DOI: 10.1039/d4tc01750a

rsc.li/materials-c

Black needle-shaped crystals of a novel Eu(II)-containing chalcogenide semiconductor, $EuHfSe_3$, have been synthesized at high temperatures using sealed-tube solid-state reaction techniques. Single crystal X-ray diffraction data (XRD) was used to characterize its structure as forming in the orthorhombic space group *Pnma* (a = 8.887(1) Å, b = 3.9300(4) Å, c = 14.3827(14) Å, and Z = 4) with the NH_4CdCl_3 structure type. The extended structure is comprised of $[HfSe_3]^{2-}$ chains which are charge balanced by Eu(II) cations. ^{151}Eu Mössbauer spectroscopic measurements were consistent with the coordination of only Eu(II) cations in bicapped trigonal prisms of $EuSe_8$. The latter polyhedra are condensed *via* face-sharing into corrugated $[EuSe_2Se_{2/2}Se_{4/4}]$ layers, yielding a magnetic substructure with Eu–Eu distances of ~3.93 Å and a longer ~4.91 Å. This structural feature of the NH_4CdCl_3-type structure has been probed for its impact on the magnetic and thermodynamic properties. Magnetic susceptibility and heat capacity measurements uncover two magnetic transitions at $T_{N1} \approx 8$ K, with glassy character, and at $T_{N1} \approx 4$ K implying a complex canted antiferromagnetic or ferrimagnetic ground state.

1. Introduction

Metal-chalcogenide semiconductors with the AMX_3 stoichiometry and group-IV M-site cations (*i.e.*, Ti, Zr and Hf) have attracted a recent surge of interest because of their promising optoelectronic properties.[1–4] These include optical absorption coefficients of greater than 10^5 cm^{-1}, relatively small effective masses of 0.3 to 0.5m_e^*, as well as small visible-light band gaps in the range of ~1.5 to 2.5 eV. Coupled with their promising kinetic stability and intense luminescence, perovskite chalcogenides appear to satisfy many of the key prerequisites for development as high efficiency photovoltaics. Many new, hypothetical compositions are predicted to exhibit relatively limited thermodynamic stability and have been difficult to prepare in high purity owing to the refractory nature of the reactants and the high reaction temperatures that are required. As a result, relatively few have been reported. For example, $SrHfCh_3$ (Ch = S or Se) and $BaHfS_3$ in distorted perovskite-type structures have been recently investigated for their semiconducting properties.[5–7] While much research has focused on the optoelectronic properties of perovskite-type chalcogenide structures, their favorable optoelectronic properties have recently been shown to extend to non-perovskite structure types.[8,9]

Eu(II)-based systems have been much less explored within the semiconducting metal chalcogenides, especially when considering the well-known similarity of its structural chemistry and ionic size with the Sr(II) cation.[10,11] These have included reports of the synthesis and structure of $EuMS_3$ (M = Zr or Hf) with the $GdFeO_3$ distorted-perovskite structure type[7,12] and $EuZrSe_3$ with the NH_4CdCl_3 structure type.[13] In addition to their potentially useful optical properties for solar energy conversion, the Eu(II)-containing chalcogenides have also received longstanding theoretical and experimental interest for their magnetic and magneto-optical properties, such as for their especially large Faraday and Kerr effects.[14,15] For example, the known Eu(II) chalcogenides, *e.g.*, EuS, EuSe and EuTe, have been investigated for their magneto-optical properties and complex, low-temperature, phase transitions (antiferromagnetic and ferromagnetic).[16–18] More broadly, and in recent years, Eu(II)-containing semiconductors have drawn significant interest as potential topological magnetic materials, such as

[a] Department of Chemistry, North Carolina State University, Raleigh, North Carolina 27695, USA. E-mail: Paul_Maggard@ncsu.edu
[b] Materials Science Center, National Renewable Energy Laboratory, Golden, Colorado 80401, USA
[c] Institut für Anorganische und Analytische Chemie, Universität Münster, Corrensstrasse 30, 48149 Münster, Germany

† Electronic supplementary information (ESI) available: The SEM data of the elemental composition, the atomic displacement parameters, the metric details of the final refined structure, and additional magnetic and thermodynamic data. CCDC 2328994. For ESI and crystallographic data in CIF or other electronic format see DOI: https://doi.org/10.1039/d4tc01750a

notably for $EuCd_2As_2$,[19,20] $Eu_5In_2Sb_6$,[21] and EuCuAs.[22] In these cases, the underlying entanglement of electronic and magnetic degrees-of-freedom can yield remarkable physical phenomena such as colossal magnetoresistance and a large topological Hall effect. It is clear that Eu(II)-based ternary semiconductors can exhibit a wide range of useful and remarkable physical properties arising from the large, localized spin moments ($S = 7/2$) and their dynamic impact on the electronic structure and optical absorption.

Recent synthetic efforts to prepare new Eu(II)-containing semiconducting materials have resulted in the new compound $EuHfSe_3$ obtained as single crystals and in high purity using solid-state reaction conditions. It represents the missing member of the $Eu^{II}MCh_3$ (M = Zr or Hf; Ch = S or Se) family with the 1 : 1 : 3 stoichiometry. Its crystal structure has been characterized by single crystal X-ray diffraction and contains $[HfSe_3]^{2-}$ chains that consist of distorted $HfSe_6$ octahedra that condense *via* their edges along the [010] direction. These chains are separated by corrugated layers of $EuSe_8$ polyhedra. The nature of the Eu(II) cations and their magnetic interactions has been probed by Mössbauer spectroscopy and temperature- and applied magnetic field-dependent magnetic susceptibility and heat capacity measurements.

2. Experimental

2.1. Materials used and synthetic procedures

The syntheses of single crystals and polycrystalline phase were carried out using the following elemental starting materials of Eu ingot (99.9% purity, Alfa Aesar), Hf powder (99.9% purity, Alfa Aesar), Sn chunk (99.99% purity, Alfa Aesar), and Se powder (99.999% purity, Alfa Aesar). Eu ingot and Hf powder are air sensitive, so all the chemicals were handled inside an Ar-filled dry glove box.

2.1.1. Synthesis of $EuHfSe_3$ single crystals. Our attempt to synthesize the Eu analog of our recently reported compound, $Ba_9Hf_3Sn_2Se_{19}$[9] produced black needle-shaped crystals of $EuHfSe_3$. The elemental starting materials of Eu (56.3 mg, 0.370 mmol), Hf (22.1 mg, 0.124 mmol), Sn (9.8 mg, 0.083 mmol), and Se (61.8 mg, 0.783 mmol) were loaded into a 6 mm outer diameter (OD) fused silica tube inside the Ar-filled glove box aiming at a composition of $Eu_9Hf_3Sn_2Se_{19}$. The tube was then evacuated for ten minutes under $\sim 10^{-4}$ torr pressure and sealed using a flame torch. The sealed reaction vessel was subjected to heat treatment inside a programmable muffle furnace and heated to 773 K in 10 h where it was annealed for 12 h before ramping to 1173 K in 10 h. The tube was then annealed for 72 h at 1173 K before cooling to 573 K using a cooling rate of 20 K h^{-1}. Finally, the furnace was shut down and allowed to cool to room temperature. The product was analyzed in an ambient atmosphere under the optical microscope revealing the presence of black needle-shape crystals along with powdered product. The needle-shaped crystals were analyzed with the help of a JEOL SEM 6010LA energy-dispersive X-ray (EDX) spectroscope using a 20 kV accelerating voltage. The EDX analysis of the needle-shaped crystals showed the presence of Eu, Hf, and Se atoms in an approximate atomic ratio of $\approx 1:1:3$ (Fig. S1, ESI†). The $EuHfSe_3$ single crystals were further reproduced using the same heating profile from a stoichiometric amount of elemental starting materials with a loaded amount of 150 mg. The compositions of $EuHfSe_3$ crystals were established using EDX analyses and unit cell determination using single crystal X-ray diffraction (SCXRD).

2.1.2. Synthesis of $EuHfSe_3$ polycrystalline phase. A two-step high-temperature solid-state synthesis method was used to synthesize pure $EuHfSe_3$ polycrystalline phase at 1173 K. At first, a stoichiometric amount of Eu (133.9 mg, 0.881 mmol), Hf (157.3 mg, 0.881 mmol), and Se (208.8 mg, 2.644 mmol) was loaded into a 12 mm outer-diameter (OD) tube inside an Ar-filled glove box. The tube was then evacuated to 10^{-4} torr and sealed using a flame torch. The sealed ampoule was then heated to 823 K in 8 h inside a muffle furnace. The temperature was held for 12 h at 823 K before ramping the temperature to 1173 K. The reaction ampoule was then annealed for 60 h before switching off the furnace and allowed to cool to room temperature. The tube was opened inside the Ar-filled glove box and the product was homogeneously ground to polycrystalline powder. The polycrystalline product was then pelletized under ~ 10 MPa pressure using a hydraulic press. Next, the pelletized product was transferred into a 12 mm OD fused silica tube and flame-sealed under 10^{-4} torr pressure. In the second step, the sealed tube was heat-treated for 72 h inside a muffle furnace. The product was ground homogeneously inside the Ar-filled glove box and the phase purity of the $EuHfSe_3$ polycrystalline phase was established using a powder X-ray diffraction (PXRD) study. Rietveld refinement of the PXRD data is provided in the ESI.†

2.2. Single crystal X-ray diffraction

The crystal structure of $EuHfSe_3$ was established using a single crystal X-ray diffraction data set at room temperature (300(2) K). A Bruker D8 Venture diffractometer equipped with a Photon III mixed mode detector was used for the intensity data collection using a graphite monochromatized Mo-Kα (λ = 0.71073 Å) radiation source. A black needle-shaped $EuHfSe_3$ crystal was mounted onto a transparent loop under Paratone-N oil and fixed onto the goniometer of the diffractometer. The crystal quality was assessed, and the unit cell was determined by a fast scan of 180 frames utilizing a frame width and exposure time of 1° and 1 s per frame, respectively. A full-intensity dataset was recorded using a working voltage of 50 kV, a current of 1.4 mA, an exposure time of 3 s per frame, a frame width of 0.5°, and a crystal-to-detector distance of 50 mm. The APEX4 software[23] was used to integrate the collected data and refine the unit cell parameters. The absorption correction was employed using the multi-scan method of the SADABS program.[24]

The XPREP program suggested a primitive (P) orthorhombic unit cell for the $EuHfSe_3$ crystal. Based on the extinction conditions, XPREP[25] suggested two space groups: *Pnma* (centrosymmetric) and $Pna2_1$ (non-centrosymmetric). The $|E^2 - 1|$ (mean intensity statistics) value of 0.882 indicated the centrosymmetric nature of the space group. So, the space group *Pnma*

was used to solve the crystal structure using the direct methods of the SHELXS program of the SHELX-14 suite of programs.[26] The initial solution showed peak heights, bond distances, and coordination environments of five crystallographically-independent atomic sites that were analyzed and further assigned to the respective atoms. The full-matrix least-squares on the F^2 method of the SHELXL program[27] was used to further refine the atomic positions, anisotropic displacement parameters, weight corrections, and scale factors. The final model provided a composition of $EuHfSe_3$ (see Table 2).

The ADDSYM program of the PLATON software package[28] suggested no missing symmetry, implying that the correct space group was found. The atomic positions of the solved structure were standardized using the STRUCTURE TIDY program.[29] The crystal structure refinement and metric details are provided in Tables 1 and 2, and the ESI.†

A room-temperature powder X-ray diffraction (PXRD) data set of the polycrystalline powder of $EuHfSe_3$ was measured using Cu-Kα radiation (λ = 1.54 Å) of a PANalytical Empyrean X-ray diffractometer. The PXRD data was collected over the 2θ range of 5° to 75° using a step size of 0.013°.

2.3. Thermodynamic and magnetic property measurements

DC magnetization and AC susceptibility measurements were performed in a quantum design physical properties measurement system (PPMS) from T = 2–400 K in applied fields up to $\mu_0 H$ = 14 T. AC susceptibility was measured with a 1.5 Oe drive current at frequencies greater than 1500 Hz and with a 5 Oe drive current at frequencies lower than 1500 Hz. Heat capacity measurements were performed on pressed pellets of powder in applied fields up to $\mu_0 H$ = 14 T. Apiezon N grease was used to adhere the pellet to the puck. Three data points were collected at each temperature; the value used was the average of the second and third data point. At $\mu_0 H$ = 0 T, data were collected up to T = 150 K; this curve was fit above T = 40 K to the Debye model with an electron contribution (eqn (1)) as a background (C_{bg}). The fit parameters were A = 0.1606 J (mol K^2)$^{-1}$, B = 317.7 J (mol K)$^{-1}$, and T_D = 212.8 K.

$$C_{bg}(T) = A \cdot T + B\left(\frac{T}{T_D}\right)^3 \int_0^{T_D/T} \frac{x^4 e^x}{(e^x - 1)^2} dx \quad (1)$$

Table 1 Crystallographic refinement and structural data for a $EuHfSe_3$ single crystal[a]

Refinement parameter	$EuHfSe_3$
a (Å)	8.8865(10)
b (Å)	3.9300(4)
c (Å)	14.3827(14)
V	502.30(9)
Z	4
ρ (g cm^{-3})	7.50
μ (mm^{-1})	54.6
$R(F)^b$	0.019
$R_w(F_o^2)^c$	0.040
S	1.00
No. of measured reflections	8451
No. of independent reflections	683
No. of refined parameters	31
Reflections with $I > 2\sigma(I)$	594
Residual electron density (min/max)	2.1/−1.4

[a] The λ = 0.71073 Å, T = 300(2) K. [b] $R(F) = \sum \| F_o| - |F_c \| / \sum |F_o|$ for $F_o^2 > 2\sigma(F_o^2)$. [c] $R_w(F_o^2) = \{\sum [w(F_o^2 - F_c^2)^2] / \sum w F_o^4\}^{1/2}$. For $F_o^2 < 0$, $w = 1/[\sigma^2(F_o^2)]$; where $P = (F_o^2 + 2F_c^2)/3$.

Table 2 Refined atomic coordinates within the $EuHfSe_3$ crystal structure

Atom	Wyckoff position	Site symmetry	x	y	z	U_{eq}
Eu(1)	4c	.m.	0.43903(5)	0.250000	0.67748(3)	0.0164(1)
Hf(1)	4c	.m.	0.16993(3)	0.250000	0.44303(2)	0.0114(1)
Se(1)	4c	.m.	0.02057(8)	0.250000	0.60822(5)	0.0096(2)
Se(2)	4c	.m.	0.15979(8)	0.250000	0.01233(6)	0.0109(2)
Se(3)	4c	.m.	0.29091(9)	0.250000	0.28171(6)	0.0120(2)

2.4. ^{151}Eu Mössbauer spectroscopy

For the ^{151}Eu Mössbauer spectroscopic investigation of the $EuHfSe_3$ sample the 21.53 keV transition of ^{151}Eu with an activity of 55 MBq (1% of the total activity of a ^{151}Sm:EuF_3 source) was used. The experiment was conducted in the usual transmission geometry. The measurement was performed with a commercial nitrogen-bath cryostat. The absorber was cooled to 78 K (liquid nitrogen), while the source was kept at room temperature. The sample was diluted with α-quartz and placed within a thin-walled PMMA container at a thickness corresponding to about 7 mg Eu cm^{-2}. Fitting of the spectrum was performed with the WinNormos for Igor7 program package[30] and the graphical editing with the program CorelDraw 2017.[31]

3. Results and discussion

3.1. Syntheses and crystal structure of $EuHfSe_3$

Initially, single crystals of $EuHfSe_3$ were serendipitously synthesized at 1173 K using a high-temperature solid-state synthesis method. The yield of the $EuHfSe_3$ crystals was ∼60% based on the loaded amount of Hf. Further, the $EuHfSe_3$ crystals were later reproduced at the nominal stoichiometry with a yield of ∼80% starting from the elements and using an identical heating profile. A black-colored polycrystalline sample of $EuHfSe_3$ was prepared at 1173 K using a two-step solid-state synthetic procedure. The phase purity of the $EuHfSe_3$ polycrystalline powder was studied using room temperature PXRD data, as provided in the ESI† in Fig. S2. Rietveld refinement of the PXRD data confirmed the formation of polycrystalline $EuHfSe_3$ with a secondary phase of EuSe (11 wt%) present in the sample (Fig. S2, ESI†).

Room temperature single-crystal XRD data of $EuHfSe_3$ showed that it crystallizes in the orthorhombic space group *Pnma* with the NH_4CdCl_3 structure type (keeping in mind that the isotype relies only in the position of the nitrogen atom, neglecting the orientation of the ammonium group).[32] The unit cell contains five crystallographically unique atomic sites (one Eu, one Hf, and three Se atoms), as listed in Table 2. A unit cell view of the $EuHfSe_3$ crystal structure is shown in Fig. 1a. The $EuHfSe_3$ crystal structure is comprised of $[HfSe_3]^{2-}$ chains which are condensed along the [010] direction. The $[HfSe_3]^{2-}$

chains are charge balanced and separated from each other by isolated Eu atoms. Each of the Hf(1) atoms is connected to three Se(1), two Se(2), and one Se(3) making distorted $Hf(1)Se_6$ octahedra units. The Eu coordination environments are shown in Fig. 1(b) and (c), respectively. Each of the $Hf(1)Se_6$ units shares four edges with adjacent four $Hf(1)Se_6$ units. Condensation of the $Hf(1)Se_6$ units leads to the formation of $[HfSe_3]^{2-}$ chains. In $EuHfSe_3$, the Hf(1)–Se distances range from 2.5572(9) Å to 2.7214(9) Å (Table 3), which can be compared with the Hf–Se distances in the previously reported compounds such as $Ba_8Hf_2Se_{11}(Se_2)$ (2.6249(4)–2.7732(4) Å),[8] $SrHfSe_3$ (2.559(2)–2.720(9) Å),[5] $Tl_2PbHfSe_4$ (2.6804(5)–2.7296(5) Å),[33] and $NaCuHfSe_3$(2.608(1)–2.788(1) Å).[34]

The magnetic substructure is comprised of Eu(II) cations coordinated within bicapped trigonal prismatic geometries, *i.e.*, $EuSe_8$ polyhedra in Fig. 1b. The Eu–Se distances (3.1568(7)–3.3617(9) Å) are listed in Table 3 and are consistent with similar distances reported in the isostructural $EuZrSe_3$ (3.147(2)–3.338(2) Å).[13] The bicapped trigonal prisms of $EuSe_8$ are further bridged into chains down the *b*-axis *via* their shared faces, illustrated in Fig. 1(b) and (c), yielding relatively short Eu–Eu distances of 3.9300(4) Å labeled with dashed lines. These chains are further bridged *via* edge sharing, with longer Eu–Eu distances of ~4.91 Å, into a corrugated layer that is charge balanced and separated by the Hf(IV) cations. The connectivity of the magnetic substructure is thus given by $[EuSe_2Se_{2/2}Se_{4/4}]$, and it forms a corrugated layer with the dimensions of a rectangular net. This structural feature of the NH_4CdCl_3-type structure has not previously been investigated for its impact on the magnetic and thermodynamic properties, as discussed below.

Given the $EuHfSe_3$ composition, the compound is found to be semiconducting with a direct transition of ~1.5 eV, Fig. S3 in the ESI.† The nominal oxidation states of the cations can be expected to be Eu(II) and Hf(IV). Bond valence sum (BVS)[35] calculations were carried out using the EXPO 2013 software[36] to estimate the oxidation states of the elements in the $EuHfSe_3$ crystal structure, and the BVS values of respective atoms are given in Table 4. The BVS values of +4 for Hf(1) and −2 for the Se atoms are in good agreement with the BVS values of these respective elements. So, the oxidation states of the Eu, Hf, and Se atoms are +2, +4, and −2, respectively, giving a charge balanced formula of $(Eu^{2+})(Hf^{4+})(Se^{2-})_3$.

Table 3 Selected interatomic distances in the $EuHfSe_3$ crystal structure

Atom pair	Distance in Å	Atom pair	Distance in Å
Hf(1)–Se(3)	2.5572(9)	Eu(1)–Se(1)	3.1664(9)
Hf(1)–Se(2)	2.6729(6) × 2	Eu(1)–Se(2)	3.2053(8) × 2
Hf(1)–Se(1)	2.6963(6) × 2	Eu(1)–Se(3)	3.2069(8) × 2
Hf(1)–Se(1)	2.7214(9)	Eu(1)–Se(2)	3.3617(9)
Eu(1)–Se(3)	3.1568(7) × 2	Eu(1)···Eu(1)	3.9300(4)

3.2. ^{151}Eu Mössbauer spectroscopy

The ^{151}Eu Mössbauer spectrum of $EuHfSe_3$ at 78 K is plotted in Fig. 2 together with a transmission integral fit. $EuHfSe_3$ shows a single signal at an isomer shift of δ = −12.33(1) mm s^{-1} indicating Eu(II) with an experimental line width of Γ = 2.25(6) mm s^{-1}. The Eu(II) ions in $EuHfSe_3$ occupy the Wyckoff site 4*c* with the non-cubic site symmetry.*m*. and are coordinated by eight short (3.157–3.362 Å Eu–Se) and one longer (3.850 Å Eu–Se) Se atoms arranged in the form of a significantly distorted multi-capped trigonal prism. Because of the electronic configuration, the quadrupole splitting in Eu(II) compounds can only arise from the lattice contribution to the electric field gradient.[37] The comparatively small lattice contribution results in an electric quadrupole splitting of ΔE_Q = 2.4(1) mm s^{-1} in $EuHfSe_3$.

The isomer shift of $EuHfSe_3$ is comparable with values of −12.10(2) and −12.18(2) mm s^{-1} that have been observed for

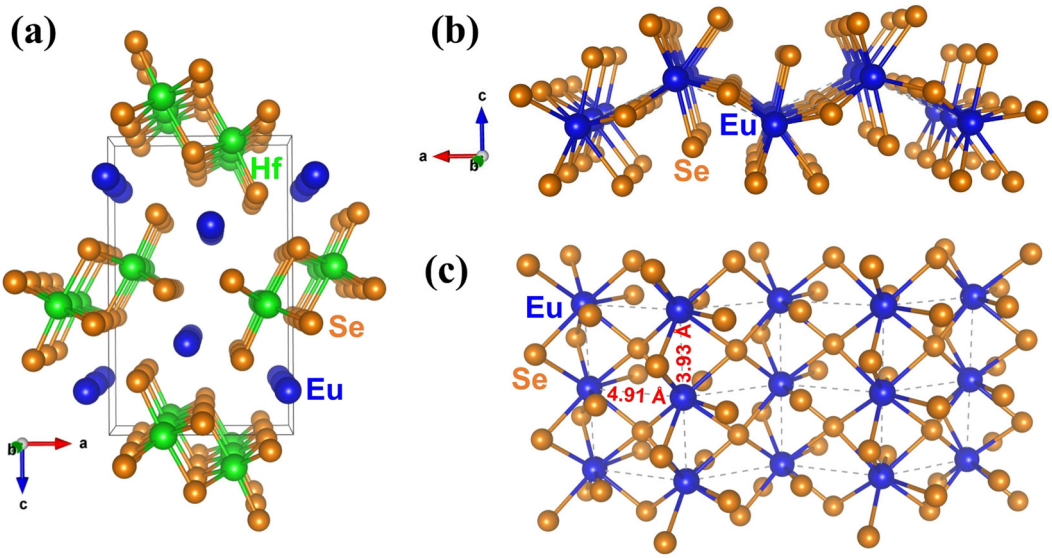

Fig. 1 A unit cell view of the $EuHfSe_3$ structure oriented approximately along the *b*-axis (a), and views of the $[EuSe_2Se_{2/2}Se_{4/4}]$ corrugated layers in the same orientation with Eu–Eu nearest-neighbor distances shown as dashed lines (b), and the same layer oriented down the *c*-axis (c).

Table 4 Bond-valence sums compared to expected oxidation states in $EuHfSe_3$

Atom	BVS value	Expected oxidation state
Eu(1)	1.84	+2
Hf(1)	4.05	+4
Se(1)	2.08	−2
Se(2)	1.93	−2
Se(3)	1.88	−2

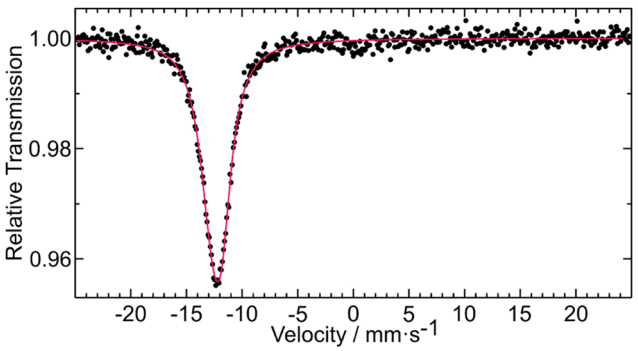

Fig. 2 Experimental (data points) and simulated (red line) ^{151}Eu Mössbauer spectrum of $EuHfSe_3$ measured at 78 K.

$EuSbSe_3$ and $EuBiSe_3$, respectively.[38] In a prior report,[39] Berkooz investigated the isomer shifts of divalent europium compounds: oxides, sulfides and selenides. The values of the selenides were in a range between −12.2 ($Eu_{0.6}Gd_{0.4}Se$) to −13.8 mm s^{-1} ($EuHo_2Se_4$ and EuY_2Se_4) relative to Eu_2O_3 ($\delta \approx$ 1.05 mm s^{-1} of Eu_2O_3 relative to ^{151}Sm:EuF_3[40]). The results were correlated with the crystal structure of the Eu(II) compounds and a monotonic increase of the isomer shifts as the mean ionic distances decrease was observed for each one of the series. The new $EuHfSe_3$ with its isomer shift ($\delta \approx -13.38$ mm s^{-1} relative to Eu_2O_3) and a mean ionic distance (Eu^{2+}–Se^{2-}) of 3.21 Å for the eight nearest neighbors fits well into the series of the selenides studied by Berkooz.[39] The average Eu–Se distance including the ninth selenium atom at 3.85 Å (8 + 1 coordination) of 3.28 Å is much larger and out of the range of the Berkooz plot. Thus, the ^{151}Eu Mössbauer spectroscopic data is sensitive to the Eu–Se distances and the ninth neighbor can only be considered as loosely bound.

3.3. Magnetic and thermodynamic properties

To study the magnetic properties of $EuHfSe_3$, DC magnetization and AC susceptibility were measured on a polycrystalline sample, as the single crystals were too small to attempt these measurements. Magnetization (M) as a function of applied magnetic field was measured at several temperatures, shown in Fig. 3a. At T = 2 K, a very small net moment is observed, and the curve has two distinct slopes in the low-field region, suggestive of multiple magnetic phenomena. At T = 6 K, the net moment is reduced, and only one slope is observed. DC susceptibility (χ) as a function of temperature in low applied fields (Fig. 3b and Fig. S4–S6, ESI†) exhibits two peaks that appear antiferromagnetic, at approximately $T_{N2} \approx 4$ K and $T_{N1} \approx 8$ K. Splitting between the zero-field-cooled (ZFC) and field-cooled (FC) data is observed below the $T_{N1} \approx 8$ K transition. Above these transitions, the field sweep is linear and consistent with paramagnetism, Fig. 3a at T = 20 K. At higher fields, both transitions are suppressed, as shown in Fig. 3b. We note that the sample used in the magnetization measurements contains ∼11 wt% EuSe, which has transitions at ∼4.6 K and ∼2.8 K.[41–43] Thus, it is possible that the transition corresponding to T_{N2} might arise in part from this impurity, although the fact that no peak at ∼2.8 K is observed in our data (see Fig. 3b, 4a, 5 and Fig. S4–S6, ESI†) implies that the magnetic contribution from EuSe is likely minimal. A Curie–Weiss fit was performed on the inverse susceptibility data collected at $\mu_0 H$ = 1 T between 51–400 K in Fig. 3c with a diamagnetic correction χ_0 of -6.3×10^{-4}. It yielded a Weiss temperature (θ) of 3.8(2) K, consistent with weak correlations. The extracted Curie constant is 8.47(2) K emu per mol, yielding an effective moment (μ_{eff}) of 8.23(1)μ_B per f.u.$^{-1}$, consistent with the expected moment for Eu(II) of 7.94μ_B. Overall, the antiferromagnetic character of the susceptibility (Fig. 3b) with the small observed net moment (Fig. 3a) and small, positive Weiss temperature suggest a canted antiferromagnetic or ferrimagnetic ground state.

To probe the dynamics of the magnetic response, AC susceptibility was measured as a function of frequency in zero

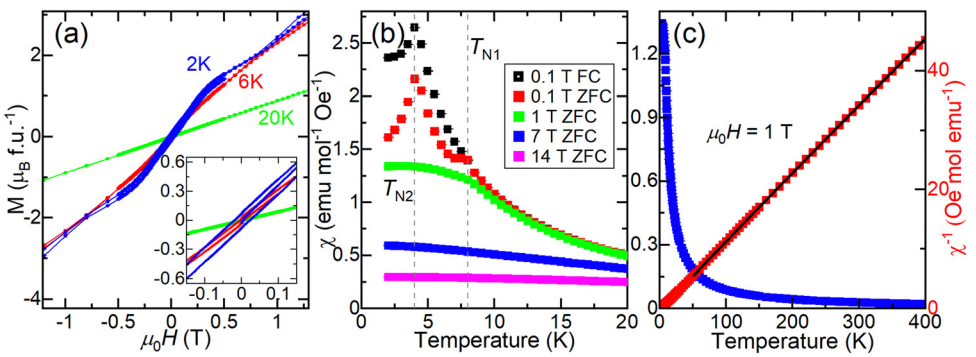

Fig. 3 DC magnetization and susceptibility of $EuHfSe_3$. (a) Magnetization (M) as a function of applied magnetic field at several temperatures. The inset shows the low-field region. (b) Magnetic susceptibility (χ) as a function of temperature at several applied fields. The dashed lines denote the transition temperatures. (c) Susceptibility and inverse susceptibility (χ^{-1}) collected in an applied field of $\mu_0 H$ = 1 T. The Curie-Weiss fit is the black line.

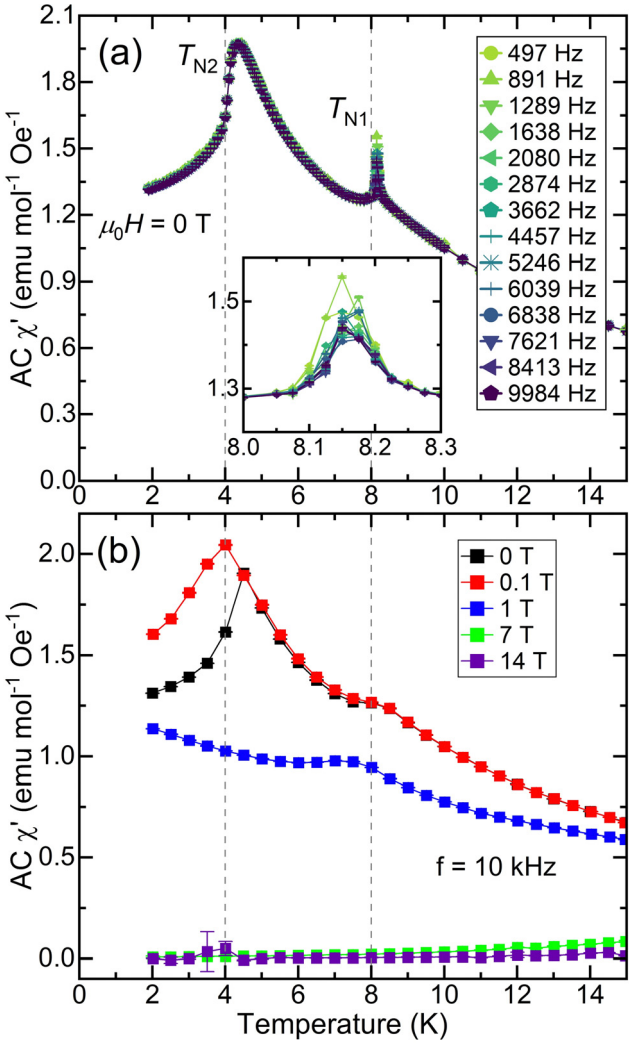

Fig. 4 AC susceptibility of $EuHfSe_3$. (a) Frequency dependence of the real part of the AC susceptibility (χ') measured in zero applied field. The inset shows the data near the T_{N1} transition. (b) Real part of the AC susceptibility measured at several applied fields. The dashed lines denote the transition temperatures.

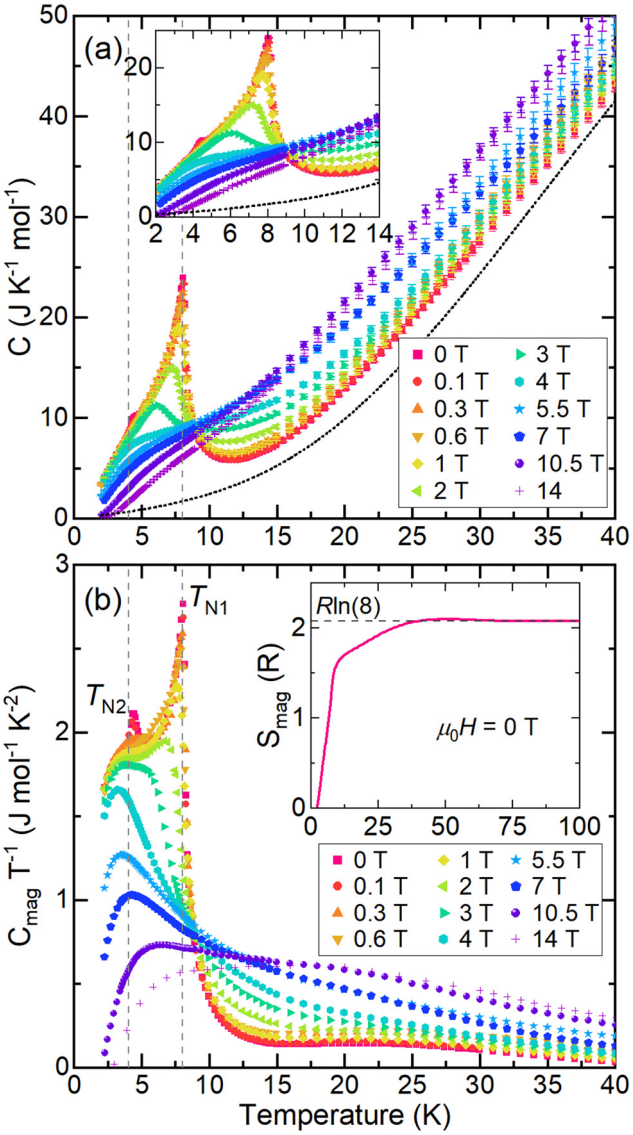

Fig. 5 Heat capacity of $EuHfSe_3$. (a) Molar heat capacity (C_p) at several applied fields; the dashed line indicates the background (C_{bg}) for the μ_0H = 0 T curve extrapolated to T = 0 K; see methods and Fig. S11 (ESI†) for details. The inset shows the low-temperature region. (b) Heat capacity related to the low-temperature peaks (C_{mag}) calculated by subtracting C_{bg} from the molar C_p. The inset shows the entropy of the low-temperature peaks (S_{mag}) normalized per formula unit for the μ_0H = 0 T curve. The vertical dashed lines denote the transition temperatures.

applied field; the real part (χ') is shown in Fig. 4a, and the imaginary part (χ''), which displays a peak at T_{N1}, is shown in Fig. S9 (ESI†). The real part of the AC susceptibility measured at high frequency, Fig. 4b, is suppressed at high fields, like the behavior seen in DC susceptibility in Fig. 3b. In the zero-field χ' data in Fig. 4a, the T_{N1} transition shifts to higher temperature with higher frequency, consistent with spin glassiness. Additionally, temperature-dependent ZFC DC susceptibility data collected at very low field (μ_0H = 0.005 T) are diamagnetic at 2 K before increasing sharply as a function of time (Fig. S7, ESI†), saturating only after approximately 40 minutes. Taken together with the observation of ZFC-FC splitting in Fig. 3b, these data suggest interesting relaxation dynamics in the magnetic ground state of $EuHfSe_3$, which likely has spin glass character.

To examine the entropy changes associated with the two low-temperature transitions, heat capacity measurements were collected on a polycrystalline sample of $EuHfSe_3$ in applied fields from 0–14 T. The background of the molar heat capacity collected at μ_0H = 0 T was fit above T = 40 K to the Debye model with an electron contribution (eqn (1); see methods and Fig. S11, ESI†); this fit is shown in Fig. 5a as a dashed line. The molar heat capacity (C_p) shown in Fig. 5a exhibits two peaks at approximately 4.2 K and 8.0 K, consistent with the magnetic measurements. These transitions shift to lower temperature when a magnetic field is applied, confirming their magnetic character, and are nearly fully suppressed at 14 T. The heat capacity related to the magnetic transitions ($C_{mag} = C_p - C_{bg}$) divided by temperature is shown in Fig. 5b. As the applied field

increases, the peak at T_{N2} is suppressed quickly, while the peak at T_{N1} broadens and shifts to lower temperature. We hypothesize that long-range ordering of $EuHfSe_3$ occurs at T_{N1}. The calculated entropy per formula unit released by these transitions for the zero-field curve by integrating C_{mag}/T is plotted as a function of temperature, in Fig. 5b (inset). The released entropy plateaus at approximately $R\ln(8)$, as shown as a dashed line in Fig. 5c, above $T_{N1} \approx 8$ K, which is consistent with the entropy expected for a Eu(II) cation ($R\ln(8)$ or 17.29 J per K per mol).

Overall, the magnetic susceptibility and thermodynamic results are consistent with the ^{151}Eu Mössbauer spectrum and confirm the presence of Eu(II) cations in the structure, *i.e.*, the effective moment is consistent with the value expected for Eu(II). An enhancement in the magnetic moment is analogous to many compounds with isoelectronic rare earth cations, such as the Gd(III) cation. The increased moment is well known in rare-earth magnetochemistry to arise from gadolinium 5d electrons that induce 4f–5d exchange interactions.[44] Eu(II) compounds have also been reported to show enhanced moments.[45] If Eu(III) cations were present, the effective moment would be suppressed, which is not observed. The magnetic susceptibility and heat capacity data indicate magnetism beyond free Eu(II) moments. Two ordering transitions are observed at $T_{N1} \approx 8$ K and $T_{N2} \approx 4$ K, although the possibility of T_{N2} arising from EuSe is not fully ruled out. The small net moment observed below T_{N1} and the small positive Weiss temperature suggests that $EuHfSe_3$ has competing interactions and a canted antiferromagnetic or ferrimagnetic ground state. In many rare-earth magnetic systems similar competing interactions have been observed as a function of temperature and magnetic field.[46–50] Typically free rare-earth ion magnetism bundled with either RKKY interactions, dipole–dipole interactions, or geometric frustration are responsible, though more complicated indirect exchange interactions stemming from f-electron and spd hybridization have been proposed.[51] In addition, recent work has demonstrated the occurrence of spin frustration in the rare-earth Yb(III)-containing oxyhalides in $S = 1/2$ square lattice antiferromagnets.[52] This work extends these investigations to the Eu(II)-containing $EuHfSe_3$, wherein the Eu(II) cations form a corrugated rectangular net (Fig. S12, ESI†) with nearest ($\sim$3.93 Å) and next-nearest ($\sim$4.91 Å) neighbors connected by Se^{2-} anions, naturally identifying an anisotropy that could be responsible for two unique magnetic correlations as shown in Fig. 1(b), (c) and in Fig. S12 (ESI†). Nonetheless, $EuHfSe_3$ orders at T_{N1} into a likely canted antiferromagnetic or ferrimagnetic structure followed by a secondary transition at T_{N2} that slightly increases the net moment. T_{N2} is suppressed with the application of a small magnetic field ($\sim$1 T) which likely bolsters the ordering at T_{N1}. Further study, particularly on single crystals to disentangle the contributions from $EuHfSe_3$ and EuSe, will be necessary to better understand the low-temperature magnetic structure and ordering of $EuHfSe_3$ as well as its relaxation dynamics and glassy character.

4. Conclusions

Single crystals and a pure polycrystalline phase of $EuHfSe_3$ were synthesized at 1173 K using sealed-tube solid-state synthesis method. Single crystal X-ray diffraction showed that the black needle-shaped crystals of $EuHfSe_3$ crystallize in the NH_4CdCl_3 structure type with orthorhombic *Pnma* symmetry and unit cell dimensions of a = 8.8865(10) Å, b = 3.9300(4) Å and c = 14.3827(14) Å. The edge-sharing Hf(1)Se_6 units form $[HfSe_3]^{2-}$ chains, which are separated by Eu(II) cations. Bond valence sums, a ^{151}Eu Mössbauer spectrum, the effective magnetic moment extracted from a Curie–Weiss fit of magnetic susceptibility data, and magnetic entropy analysis indicate full consistency with the Eu(II) oxidation state. The Eu(II) cations are coordinated within $EuSe_8$ bicapped trigonal prisms that are condensed *via* face-sharing into corrugated $[EuSe_2Se_{2/2}Se_{4/4}]$ layers, yielding a magnetic substructure with Eu–Eu distances of $\sim$3.93 Å and a longer $\sim$4.91 Å. Polycrystalline magnetic susceptibility and heat capacity measurements uncover two magnetic transitions at low temperature: the primary transition occurs at $T_{N1} \approx 8$ K, along with a secondary transition at $T_{N2} \approx 4$ K; some contribution arising from an EuSe impurity cannot be fully ruled out. $EuHfSe_3$ has a complex magnetic ground state that is likely canted antiferromagnetic or ferrimagnetic, as there is a small net moment below T_{N1}. In addition, the data suggest interesting magnetic relaxation dynamics and spin glass character at low temperature. Overall, $EuHfSe_3$ is a novel Eu(II)-containing chalcogenide with intriguing and complex low-temperature magnetic behavior.

Author contributions

Formal analysis, investigation, visualization, and writing – all authors; project administration and supervision – RP, RWS and PAM.

Data availability

The data supporting this article have been included as part of the ESI.†

Conflicts of interest

There are no conflicts to declare.

Acknowledgements

The authors acknowledge primary support of this work from the National Science Foundation (DMR-2317605). This work was also authored in part by the National Renewable Energy Laboratory, operated by Alliance for Sustainable Energy, LLC, for the U.S. Department of Energy (DOE) under Contract No. DE-AC36-08GO28308. Single crystal X-ray characterization was performed in part by the Molecular Education, Technology and Research Innovation Center (METRIC) at NC State University, which is supported by the State of North Carolina. Funding for magnetometry and heat capacity provided by the U.S. Department of Energy, Office of Science, Basic Energy Sciences, Division of Materials Science, through the Office of Science Funding Opportunity Announcement (FOA) Number DE-FOA-

0002676: Chemical and Materials Sciences to Advance Clean-Energy Technologies and Transform Manufacturing. The views expressed in the article do not necessarily represent the views of the DOE or the U.S. Government.

References

1 P. Basera and S. Bhattacharya, Chalcogenide Perovskites (ABS_3; A = Ba, Ca, Sr; B = Hf, Sn): An Emerging Class of Semiconductors for Optoelectronics, *J. Phys. Chem. Lett.*, 2022, **13**, 6439–6446.

2 R. Raj, R. Singh and M. Guin, Chalcogenide Perovskite, An Emerging Photovoltaic Material: Current Status and Future Perspectives, *ChemistrySelect*, 2023, **8**, e202303550.

3 D. Tiwari, O. S. Hutter and G. Longo, Chalcogenide Perovskites for Photovoltaics: Current Status and Prospects, *JPhys Energy*, 2021, **3**, 034010.

4 K. V. Sopiha, C. Comparotto, J. A. Márquez and J. S. Scragg, Chalcogenide Perovskites: Tantalizing Prospects, Challenging Materials, *Adv. Opt. Mater.*, 2022, **10**(1–27), 2101704.

5 N. A. Moroz, C. Bauer, L. Williams, A. Olvera, J. Casamento, A. A. Page, T. P. Bailey, A. Weiland, S. S. Stoyko, E. Kioupakis, C. Uher, J. A. Aitken and P. F. P. Poudeu, Insights on the Synthesis, Crystal and Electronic Structures, and Optical and Thermoelectric Properties of $Sr_{1-x}Sb_xHfSe_3$ Orthorhombic Perovskite, *Inorg. Chem.*, 2018, **57**, 7402–7411.

6 K. Hanzawa, S. Iimura, H. Hiramatsu and H. Hosono, Material Design of Green-Light-Emitting Semiconductors: Perovskite-Type Sulfide $SrHfS_3$, *J. Am. Chem. Soc.*, 2019, **141**, 5343–5349.

7 R. Lelieveld and D. J. W. IJdo, Sulphides with the $GdFeO_3$ Structure, *Acta Crystallogr., Sect. B: Struct. Crystallogr. Cryst. Chem.*, 1980, **36**, 2223–2226.

8 S. Jana, E. A. Gabilondo and P. A. Maggard, Two New Multinary Chalcogenides with $(Se_2)^{2-}$ Dimers: $Ba_8Hf_2Se_{11}(Se_2)$ and $Ba_9Hf_3Se_{14}(Se_2)$, *J. Solid State Chem.*, 2024, **329**, 124376.

9 S. Jana, E. Gabilondo, S. McGuigan and P. A. Maggard, Syntheses, Crystal Structures, and Electronic Structures of Quaternary Group IV-Selenide Semiconductors, *Inorg. Chem.*, 2024, **63**, 6474–6482.

10 G. J. McCarthy and J. E. Greedan, Complex Oxides Containing Divalent Europium. I. Guidelines for the Prediction of New Phases. Application to the Phases of the Type $EuMO_3$, *Inorg. Chem.*, 1975, **14**, 772–775.

11 J. E. Greedan, G. J. McCarthy and C. Sipe, Complex Oxides Containing Divalent Europium. II. $Eu(M,M')O_3$ Phases, *Inorg. Chem.*, 1975, **14**, 775–779.

12 S.-P. Guo, Y. Chi, J.-P. Zou and H.-G. Xue, Crystal and Electronic Structures, and Photoluminescence and Photocatalytic Properties of α-$EuZrS_3$, *New J. Chem.*, 2016, **40**, 10219–10226.

13 A. Mar, and J. A. Ibers, Structure of Europium Zirconium Selenide, $EuZrSe_3$, *Acta Crystallogr.*, 1992, **C48**, 771–773.

14 J. C. Suits, B. E. Argyle and M. J. Freiser, Magneto-Optical Properties of Materials Containing Divalent Europium, *J. Appl. Phys.*, 1966, **37**, 1391–1397.

15 Y. Hasegawa, T.-a Adachi, A. Tanaka, M. Afzaal, P. O'Brien, T. Doi, Y. Hinatsu, K. Fujita, K. Tanaka and T. Kawai, Remarkable Magneto-Optical Properties of Europium Selenide Nanoparticles with Wide Energy Gaps, *J. Am. Chem. Soc.*, 2008, **130**, 5710–5715.

16 T. R. McGuire, B. E. Argyle, M. W. Shafer and J. S. Smart, Magnetic Properties of Some Divalent Europium Compounds, *J. Appl. Phys.*, 1963, **34**, 1345–1346.

17 W. Zinn, Microscopic Studies of Magnetic Properties, and Interactions Recent Results on Europium Monochalcogenides, *J. Magn. Magn. Mater.*, 1976, **3**, 23–36.

18 J. O. Dimmock, Optical Properties of the Europium Chalcogenides, *IBM J. Res. Dev.*, 1970, **14**, 301–308.

19 J.-Z. Ma, S. M. Nie, C. J. Yi, J. Jandke, T. Shang, M. Y. Yao, M. Naamneh, L. Q. Yan, Y. Sun, A. Chikina, V. N. Strocov, M. Medarde, M. Song, Y.-M. Xiong, G. Xu, W. Wulfhekel, J. Mesot, M. Reticcioli, C. Franchini, C. Mudry, M. Müller, Y. G. Shi, T. Qian, H. Ding and M. Shi, Spin Fluctuation Induced Weyl Semimetal State in the Paramagnetic Phase of $EuCd_2As_2$, *Sci. Adv.*, 2019, **5**, eaaw4718.

20 I. Schellenberg, U. Pfannenschmidt, M. Eul, C. Schwickert and R. Pöttgen, A ^{121}Sb and ^{151}Eu Mössbauer Spectroscopic Investigation of $EuCd_2X_2$ (X = P, As, Sb) and $YbCd_2Sb_2$, *Z. Anorg. Allg. Chem.*, 2011, **637**, 1863–1870.

21 M. V. A. Crivillero, S. Röβler, S. Granovsky, M. Doerr, M. S. Cook, P. F. S. Rosa, J. Müller and S. Wirth, Magnetic and Electronic Properties Unveil Polaron Formation in $Eu_5In_2Sb_6$, *Sci. Rep.*, 2023, **13**, 1597.

22 S. Roychowdhury, K. Samanta, P. Yanda, B. Malaman, M. Yao, W. Schnelle, E. Guilmeau, P. Constantinou, S. Chandra, H. Borrmann, M. G. Vergniory, V. Strocov, C. Shekhar and C. Felser, Interplay between Magnetism and Topology: Large Topological Hall Effect in an Antiferromagnetic Topological Insulator, EuCuAs, *J. Am. Chem. Soc.*, 2023, **145**, 12920–12927.

23 *Bruker APEX4 Version 2009.5-1 Data Collection and Processing Software*, Bruker Analytical X-Ray Instruments, Inc., Madison, WI, 2009.

24 G. M. Sheldrick, *SADABS*, 2008.

25 G. M. Sheldrick, *XPREP Version 2008/2*, Bruker AXS Inc., Madison, 2018.

26 G. M. Sheldrick, A Short History of SHELX, *Acta Crystallogr., Sect. A: Found. Crystallogr.*, 2008, **64**, 112–122.

27 G. M. Sheldrick, Crystal Structure and Refinement with SHELXL, *Acta Crystallogr., Sect. C: Struct. Chem.*, 2015, **71**, 3–8.

28 A. L. Spek, Single-Crystal Structure Validation with the Program PLATON, *J. Appl. Crystallogr.*, 2003, **36**, 7–13.

29 L. M. Gelato and E. Parthé, STRUCTURE TIDY – A Computer Program to Standardize Crystal Structure Data, *J. Appl. Crystallogr.*, 1987, **20**, 139–143.

30 R. A. Brand, *WinNormos for Igor7 (version for Igor 7.010 or above: 01/03/2020)*, Universität Duisburg, Duisburg, Germany, 2020.

31 *CorelDRAW Graphics Suite 2017 (version 19.0.0.328)*, Corel Corporation, Ottowa, Ontario, Canada, 2017.

32 H. Brasseur and L. Pauling, The Crystal Structure of Ammonium Cadmium Chloride, NH_4CdCl_3, *J. Am. Chem. Soc.*, 1938, **60**(12), 2886–2890.

33 C. R. Sankar, A. Assoud and H. Kleinke, New Layered-Type Quaternary Chalcogenides, Tl_2PbMQ_4 (M = Zr, Hf; Q = S, Se): Structure, Electronic Structure, and Electrical Transport Properties, *Inorg. Chem.*, 2013, **52**, 13869–13874.

34 K. O. Klepp and D. Sturmayr, Crystal Structure of Sodium Copper Triselenohafnate(IV), $NaCuHfSe_3$, *Z. Kristallogr. - New Cryst. Struct.*, 1997, **212**, 75.

35 N. E. Brese and M. O'Keeffe, Bond-Valence Parameters for Solids, *Acta Crystallogr., Sect. B: Struct. Sci.*, 1991, **47**, 192–197.

36 A. Altomare, C. Cuocci, C. Giacovazzo, A. Moliterni, R. Rizzi, N. Corriero and A. Falcicchio, EXPO2013: A Kit of Tools for Phasing Crystal Structures from Powder Data, *J. Appl. Crystallogr.*, 2013, **46**, 1231–1235.

37 N. N. Greenwood and T. C. Gibb, *Mössbauer Spectroscopy*, Chapman & Hall, London, 1971.

38 F. M. Schappacher, R. Pöttgen, J. G. Bang and T. E. Albrecht-Schmitt, ^{151}Eu and ^{121}Sb Mössbauer Spectroscopy of $EuSbSe_3$ and $EuBiSe_3$, *J. Solid State Chem.*, 2007, **180**, 3035–3038.

39 O. Berkooz, Isomer Shifts of ^{151}Eu in Divalent Europium Compounds, *J. Phys. Chem. Solids*, 1969, **30**, 1763–1767.

40 N. R. Large, R. J. Bullock, P. Glentworth and D. A. Newton, Isomer Shift of the Mössbauer Spectrum of $^{151}EuF_3$, *Phys. Lett.*, 1969, **29A**, 352–353.

41 P. Wachter, *Handbook on the Physics and Chemistry of Rare Earths*, Elsevier, *Amsterdam*, 1979, ch. 19, vol. 2, pp. 507–574.

42 D. X. Li, T. Yamamura, S. Nimori, Y. Homma, F. Honda and D. Aoki, Giant and isotropic low temperature magnetocaloric effect in magnetic semiconductor EuSe, *Appl. Phys. Lett.*, 2013, **102**(1–4), 152409.

43 R. Griessen, M. Landolt and H. R. Ott, A new antiferromagnetic phase in EuSe below 1.8 K, *Solid State Commun.*, 1971, **9**, 2219–2223.

44 G. Czjzek, V. Oestreich, H. Schmidt, K. Łątka and K. Tomalain, A study of compounds GdT_2Si_2 by Mössbauer Spectroscopy and by bulk magnetization measurements, *J. Magn. Magn. Mater.*, 1989, **79**, 42–56.

45 R. Pöttgen and D. Johrendt, Equiatomic intermetallic europium compounds: syntheses, crystal chemistry, chemical bonding, and physical properties, *Chem. Mater.*, 2000, **12**, 875–897.

46 I. A. Leahy, K. Feng, R. Dery, R. Baumbach and M. Lee, Field-induced magnetic states in the metallic rare-earth layered triangular antiferromagnet $TbAuAl_4Ge_2$, *Phys. Rev. B*, 2022, **106**, 094426.

47 K. Feng, I. A. Leahy, O. Oladehin, K. Wei, M. Lee and R. Baumbach, Magnetic ordering in $GdAuAl_4Ge_2$ and $TbAuAl_4Ge_2$: Layered compounds with triangular lanthanide nets, *J. Magn. Magn. Mater.*, 2022, **564**, 170006.

48 M. O. Ajeesh, S. K. Kushwaha, S. M. Thomas, J. D. Thompson, M. K. Chan, N. Harrison, J. M. Tomczak and P. F. S. Rosa, Localized *f*-electron magnetism in the semimetal $Ce_3Bi_4Au_3$, *Phys. Rev. B*, 2023, **108**, 245125.

49 S. L. Bud'ko, P. C. Canfield, C. H. Mielke and A. H. Lacerda, Anisotropic magnetic properties of light rare-earth diantimonides, *Phys. Rev. B: Condens. Matter Mater. Phys.*, 1998, **57**, 13624.

50 S. Lucas, K. Grube, C.-L. Huang, A. Sakai, S. Wunderlich, E. L. Green, J. Wosnitza, V. Fritsch, P. Gegenwart, O. Stockert and H. V. Löhneysen, Entropy Evolution in the Magnetic Phases of Partially Frustrated CePdAl, *Phys. Rev. Lett.*, 2017, **118**, 107204.

51 L. Peters, S. Ghosh, B. Sanyal, C. van Dijk, J. Bowlan, W. de Heer, A. Delin, I. Di Marco, O. Eriksson, M. I. Katsnelson, B. Johansson and A. Kirilyuk, Magnetism and exchange interaction of small rare-earth clusters; Tb as a representative, *Nat. Sci. Rep.*, 2016, 19676.

52 P. Park, G. Sala, T. Proffen, M. B. Stone, A. D. Christianson and A. F. May, Quantum magnetism in the frustrated square lattice oxyhalides $YbBi_2IO_4$ and $YbBi_2ClO_4$, *Phys. Rev. B*, 2024, **109**, 014426.